



## OPEN IR thermography & NN models for damaged component thickness detection

Chunming Ai<sup>1,2</sup>, Haichuan Lin<sup>1,2</sup>✉ & Pingping Sun<sup>3</sup>

To achieve rapid detection of damage thickness in metal components using infrared thermography, a combination of heat transfer theory and image theory was employed. This involved theoretical analysis, finite element numerical simulation, a BP neural network prediction model, and infrared thermography experiments. Infrared thermal wave experiments were conducted under different heating temperatures. By analyzing the obtained temperature data, the response characteristics of surface temperature distribution to component thickness were investigated. The COMSOL numerical simulation software was used to simulate the surface temperature of the metal components. The bevel-cut metal components were heated to 80 °C, 105 °C, and 130 °C, and the fitted experimental temperature data were analyzed in conjunction with the simulated temperature data of the bevel-cut metal components. It was found that the fitted experimental temperature rise curve aligned with the simulated temperature rise curve trend. A comparative analysis of the simulation results and experimental values showed that the simulated temperature rise curve was basically consistent with the fitted experimental temperature curve, validating the feasibility of using numerical simulation as a substitute for experiments. The numerical simulation data were divided into a training set and a prediction set in an 8:2 ratio. Through training with the BP neural network, the predicted data were found to be basically consistent with the experimental data, verifying the feasibility of using the BP neural network for rapid detection of damage thickness in metal components. This laid the foundation for the subsequent promotion and application of BP neural network technology for rapid detection of damage thickness in metal components. This study holds significant importance for the application of neural network-based rapid detection technology for metal component thickness in the engineering field.

**Keywords** Defect thickness detection, Infrared thermal wave nondestructive testing, COMSOL heat transfer simulation, BP neural network, Rapid detection

Infrared thermography technology, with its advantages of non-contact, non-destructive nature, high reliability, and suitability for large-area detection, has been widely applied in fields such as mechanical engineering<sup>1</sup>, energy conservation<sup>2</sup>, biology<sup>3</sup>, cultural heritage<sup>4</sup>, environmental science<sup>5</sup>, medicine<sup>6</sup>, electronics<sup>7</sup>, heat transfer<sup>8</sup>, chemistry<sup>9</sup>, physiology<sup>10</sup>, and increasingly, in the study of different types of materials<sup>11</sup>. Infrared thermographic technology is a non-destructive testing method for evaluating the condition of a sample by measuring its surface temperature field. As a non-contact detection method, it does not cause damage to the sample. However, this method requires consideration of factors such as the testing environment and temperature<sup>12–19</sup>. It is not feasible to determine the thickness of metal components solely based on their temperature obtained through infrared thermography, due to the limitations of infrared thermographic technology in terms of accuracy and rapid detection. To utilize the temperature data rapidly acquired by infrared thermography for detecting the thickness of metal components, it is advisable to integrate a neural network model. By employing the neural network model, the relationship between “temperature and thickness” can be established and a relevant database can be created, thereby achieving the purpose of rapid detection of the thickness of technical components. Currently, BP neural network technology is highly stable<sup>20</sup> and possesses data recognition and simulation capabilities. When dealing with non-linear relationships, the advantages of BP neural networks become even more pronounced<sup>21</sup>. BP neural networks can effectively reduce the influence of other factors and serve as a model that ensures overall objectivity<sup>22</sup>. By combining BP neural networks with infrared thermographic technology, precise and rapid

<sup>1</sup>College of Safety Science and Engineering, Liaoning Technical University, Huludao 125000, China. <sup>2</sup>Key Laboratory of Thermal Disaster and Prevention, Ministry of Education, Huludao 125000, China. <sup>3</sup>Tianjin Bohai Polytechnic College, No. 508, Jinyu Road, Beichen District, Tianjin 300402, China. ✉email: lhc19990512@163.com

detection of the thickness of metal components can be achieved. This method not only ensures measurement accuracy but also improves detection efficiency.

Numerous scholars at home and abroad have conducted extensive research on BP neural network models. Alnaggar et al.<sup>23</sup> leveraged deep neural networks to address challenges such as numerous model parameters and complex modeling. Song Ming et al.<sup>24</sup> proposed a method to obtain the elastoplastic mechanical properties of materials by combining artificial intelligence BP networks, small punch testing, and finite element simulation to determine the material's "stress-strain" curve. Zhang Lingyun et al.<sup>25</sup> took aircraft wing ribs as their research object and predicted the springback of rubber bladder-formed aircraft wing rib convex flanges by combining finite element simulation and neural networks. Xie Peng et al.<sup>26</sup> conducted research on predicting the remaining strength of externally corroded submarine pipelines based on deep learning. Chu Linhua et al.<sup>27</sup> employed deep learning methods to train a prediction model for the "process-stress amplitude-fatigue life" during the cold rolling of zirconium alloy tubing. Guo Hong et al.<sup>28</sup> proposed a tool wear prediction method that combines multi-sensor feature fusion with BP neural networks. The dimensionality-reduced fused features were input into a well-established BP neural network, and through nonlinear simulation analysis, wear amount prediction was achieved. Zhang Yue et al.<sup>29</sup> introduced a tire wear detection algorithm based on BP neural networks, constructing an eight-layer neural network to learn from the training set and test it with the test set, achieving errors within 0.4 mm and accurately predicting tire wear during operation. Huang Yao et al.<sup>30</sup> addressed the issue of wear prediction in extrusion molds by importing experimental data from finite element simulations into a BP neural network model for training. They predicted the wear values at various nodes of the extrusion mold. By comparing the predicted values from the BP neural network model, the calculated values from the finite element method, and the actual wear values, they found that the trained BP neural network model exhibited higher accuracy. Zhang Wei et al.<sup>31</sup> investigated the influence of milling surface characterization parameters on milling wear and established a milling surface wear resistance prediction model based on BP neural networks. They input parameters such as the maximum height, maximum peak height, maximum pit height, minimum autocorrelation length, and surface feature height ratio of the milling surface into the milling surface wear resistance prediction model for training and learning. Comparison of the predicted wear amount with the actual wear value showed that the minimum error was only 6.18%. Cao Yuanxun et al.<sup>32</sup> established a BP neural network abrasive belt wear rate model to predict the wear degree of abrasive belts. The results indicated that the BP neural network could quickly and accurately predict the abrasive belt wear rate. An Hua et al.<sup>33</sup> proposed a tool wear condition monitoring method based on the BP neural network model. They used the BP neural network model to train and learn a large number of significant feature samples of original cutting force signals and their corresponding tool wear values as inputs to predict the tool wear values. Zhao et al.<sup>34</sup> constructed a finite Ridgelet neural network optimized by the improved firefly algorithm. The prediction procedure of hydrogen pipeline is designed. It can effectively predict the safety status of the hydrogen gas pipeline.

According to the relevant neural network literature<sup>35–38</sup>, there are few studies on the rapid detection of the thickness of damaged metal members through the neural network in the defect thickness detection. Therefore, in this paper, the excitation temperature is controlled to detect the metal defect thickness by combining the technology of infrared thermal wave technology and finite element simulation and BP neural network prediction model. And through COMSOL finite element simulation to verify the correlation with the experimental results, resulting in a database of "excitation temperature-metal thickness". Follow-up the data obtained into the BP neural network prediction model for training and prediction, verify the neural network can quickly detect the feasibility of damage metal thickness, realize the rapid detection of metal component defects, for the neural network damage metal component thickness rapid nondestructive testing technology in the field of engineering application provide reference.

## Experiment and methodology

### Defect detection method

As one of the non-destructive testing techniques, infrared thermography detection operates by injecting a high-energy infrared pulse into the tested sample within a short period of time. Due to the inhomogeneity of the sample's material and shape (defects), the temperatures of different regions of the sample will vary under the influence of thermal conductivity and thermal diffusion<sup>39,40</sup>. When heat from an excitation source is applied to an obliquely cut metal plate, it conducts heat along the thickness direction, temporarily ignoring heat transfer along the lateral or lengthwise directions, thus making mathematical analysis and calculations more straightforward. The principle of heat transfer is illustrated in Fig. 1.

It can be seen from Fig. 1 that B is the heat source at one point in the sample and the temperature after time  $t$  at point A, whose temperature expression is as follows:

$$T_B(A, t) = T_A e^{-\frac{h}{\mu}} \cos(\omega t - \frac{h}{\mu}) \quad (1)$$

Where:  $T_B(A, t)$  is the temperature after time  $t$  of point A,  $T_A$  is the initial heating temperature of point A;  $h$  is the distance between two points;  $\omega$  is the natural frequency of the sample; Among  $\mu = \sqrt{2\alpha/\omega}$ ;  $\alpha$  is the thermal diffusivity of the material.

As can be seen from Fig. 1 and Eq. (1), under the same heating temperature, when the thickness  $h'$  between two points is less than  $h$ , the temperature relationship at point B is  $T_{B'} > T_B$ . This indicates that the different thicknesses of the iron plate will affect the temperature of the sample after excitation.

After the heat source A starts to stimulate the sample, the different lengths of heat conduction paths within the sample result in temperature variations for different thicknesses, thus creating temperature differences.

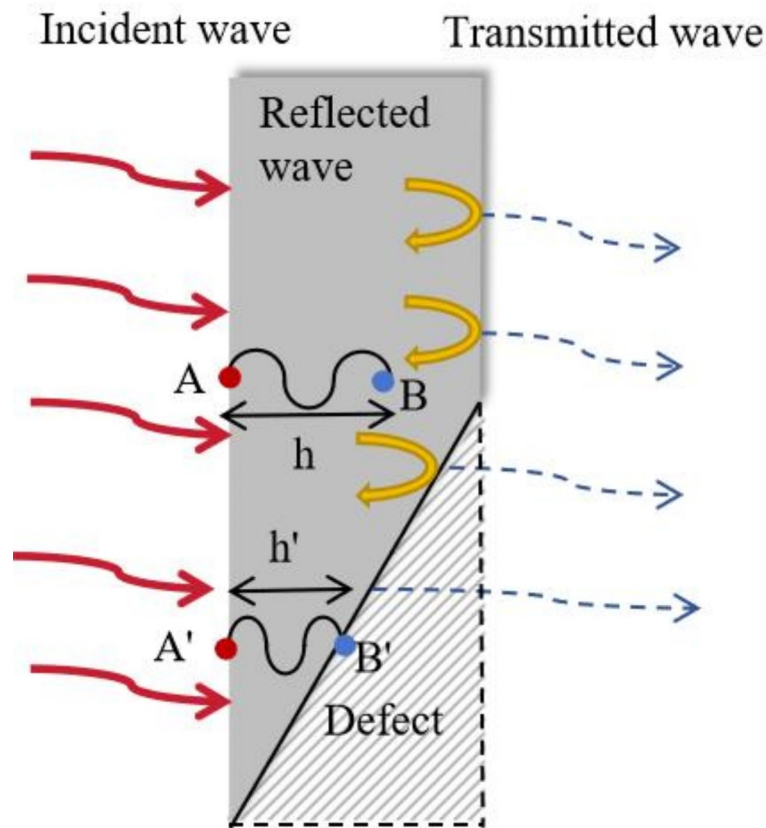


**Fig. 1.** Principle of heat transfer.

### Infrared heat wave experiment

The material selected is a 50 mm x 50 mm x 2 mm iron plate, which undergoes an oblique cutting and wear process to form a trapezoidal cross-section. This is done to enable simultaneous observation of temperatures in both the damaged and undamaged regions during the excitation of the trapezoidal iron plate, thereby allowing for the acquisition of temperature difference data. The trapezoidal iron plate is divided into six thickness intervals: 2 mm–1.8 mm, 1.8 mm–1.73 mm, 1.73 mm–1.66 mm, 1.66 mm–1.44 mm, 1.44 mm–1.19 mm, and 1.19 mm–0.7 mm (as shown in Fig. 3). Subsequently, a fixed heating temperature is applied to the sample as thermal excitation, and the UTi260A infrared thermal imager is used to record thermal images from the front.

As shown in Fig. 2, as the heating temperature continues to rise, the temperature rise rate on the oblique section is faster, and defects become more pronounced. This is due to the different heat conduction paths when heating the iron plate. As a special area of the iron plate, the geometry and surface condition of the oblique section make it easier for heat to accumulate and transmit rapidly in this area. The temperature rise rate on the oblique surface is more significant than that on other surfaces. Therefore, the degree of wear can be quantified by calculating the temperatures in defective and non-defective areas, and the temperature values can serve as an important indicator of the wear condition of the iron plate.

### Establishment and analysis of finite element model

#### Mesh generation and material selection

Establish four models of metal components with different thicknesses, using Structural steel as the material. Conduct mesh generation on the models, where the 2 mm model has 323,444 tetrahedral mesh elements and 159,632 triangular mesh elements, with an average element quality of 0.5871; the 3 mm model has 221,256 tetrahedral mesh elements and 92,848 triangular mesh elements, with an average element quality of 0.6069; the 4 mm model has 217,688 tetrahedral mesh elements and 63,668 triangular mesh elements, with an average element quality of 0.6239; and the 5 mm model has 214,310 tetrahedral mesh elements and 45,986 triangular mesh elements, with an average element quality of 0.641. To better observe the temperature changes corresponding to different thicknesses, finer mesh generation is applied to thinner areas. A reasonable number of mesh elements not only saves computer resources and increases computation speed but also ensures computational accuracy. The mesh generation is illustrated in Fig. 3.

#### Finite element simulation for thermal distribution

In the infrared thermal wave experiment, heat transfer primarily occurs through thermal radiation from the excitation source to the air, and then through convective heat transfer between the air and the test specimen,

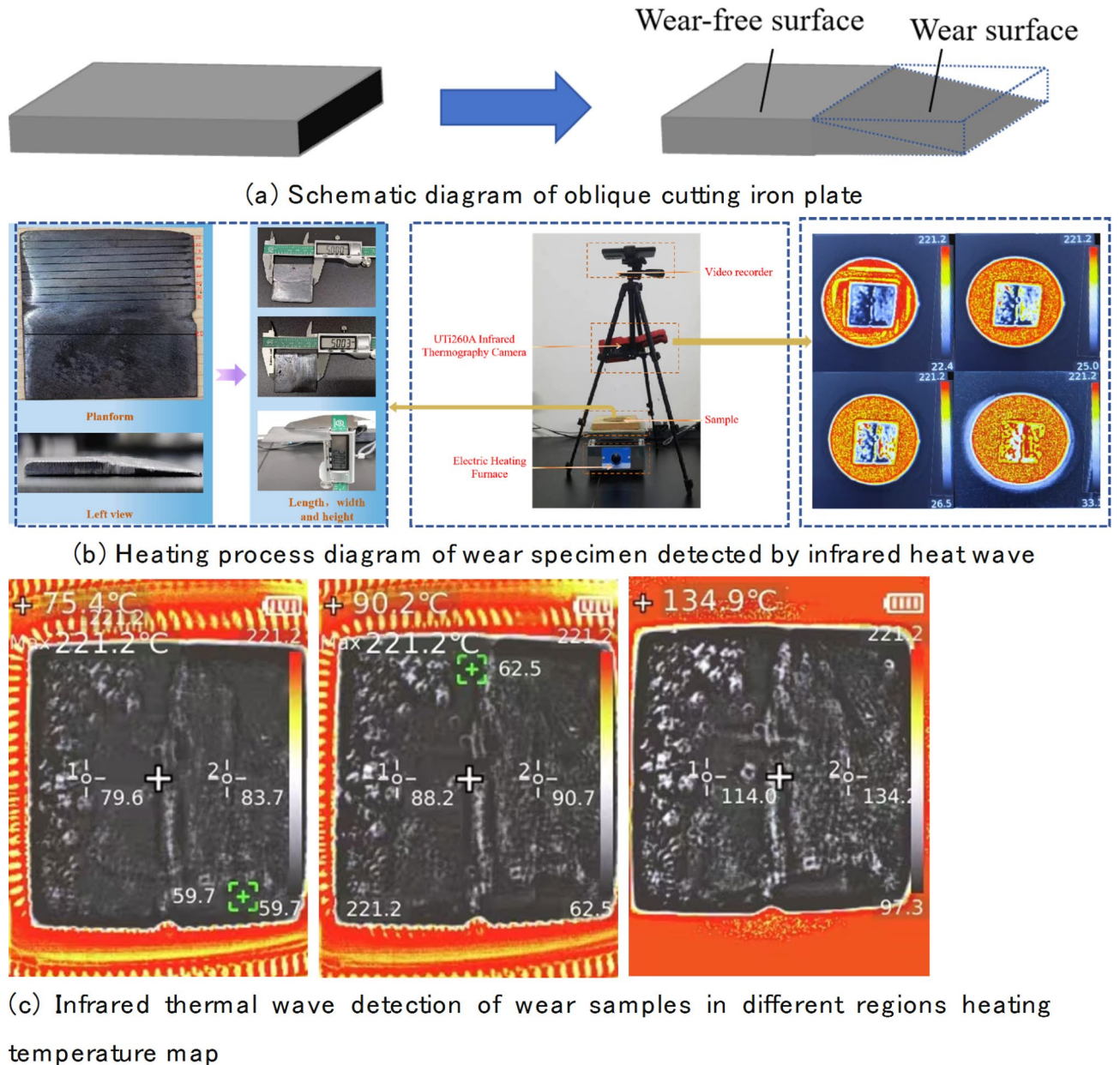


**Fig. 2.** Infrared heat wave experiment.

thereby heating the test specimen. To simulate the loading of the excitation source in the experiment, the heat transfer coefficient  $h$  in the simulation model is set to  $750 \text{ W}/(\text{m}^2\text{k})$ , and the ambient temperature is set to  $20^\circ\text{C}$ . Through simulation analysis, the thermal distribution contour plot of the finite element model can be obtained, as shown in Fig. 4.

#### Correlation analysis between finite element simulation and experimental results

The 2 mm miter wear plate was heated to  $80^\circ\text{C}$ ,  $105^\circ\text{C}$ , and  $130^\circ\text{C}$ . By combining and analyzing the experimental temperature data with the simulated temperature data for the 2 mm miter wear plate, it was found that the trend of the experimental temperature rise curve was consistent with the simulated temperature rise curve, as shown in Fig. 5.

Through the experiment, the iron plates with different wear degrees were heated, and the experimental data obtained provided the verification basis for the subsequent numerical simulation, ensuring the accuracy and reliability of the simulation results. The numerical simulation is consistent with the experimental results, which indicates that the numerical simulation can be an effective supplement or substitute for the experiment.

Through numerical simulations, the temperature distribution can be directly related to the material thickness. This method not only improves the measurement efficiency, but also reduces the human error. Based on a large number of simulation and experimental data, the “excitation temperature-metal thickness”

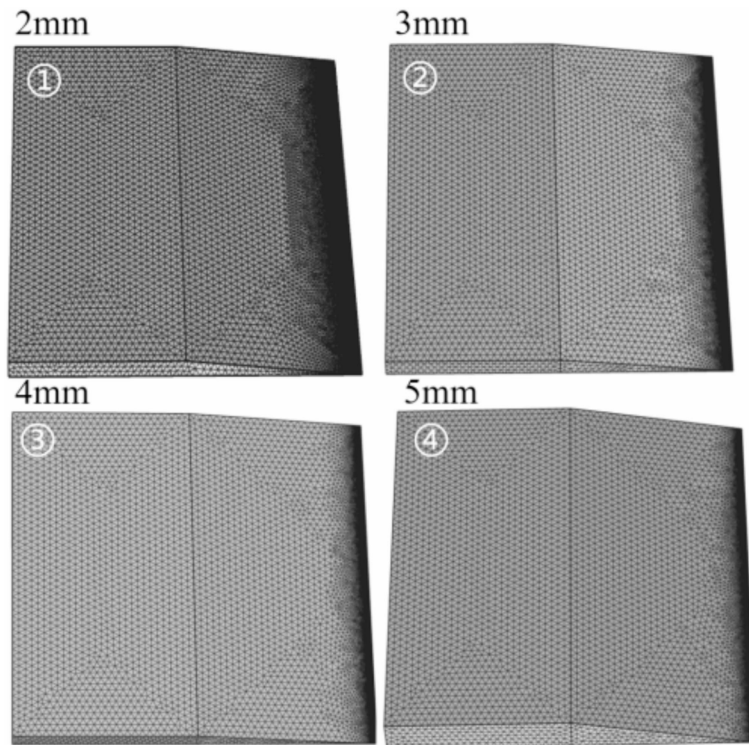


**Fig. 3.** Finite element model of 2–5 mm ferromagnetic material diagonal wear plate.

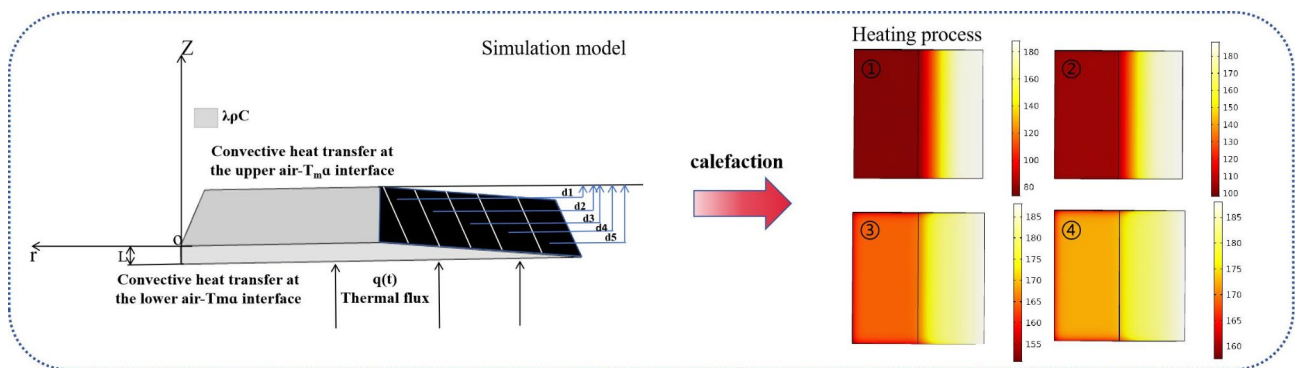


**Fig. 4.** Simulation of heat distribution of mitre cut wear plate of iron plate material.

database is constructed. In the field of infrared detection, the thickness of the measured material can be quickly and accurately inferred, which provides favorable support for the development of nondestructive detection technology.

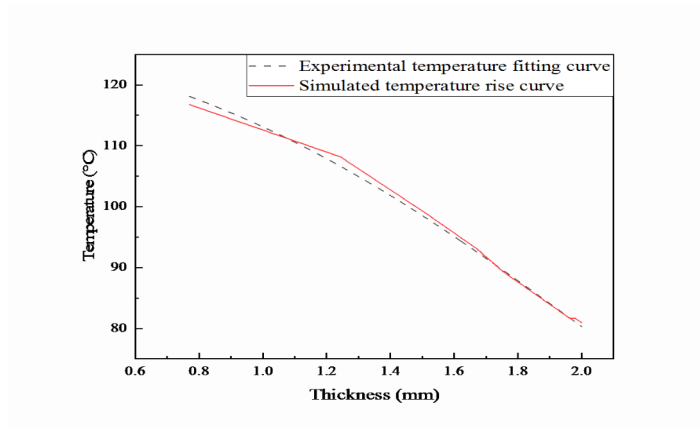
**Temperatures of different wear thicknesses at various heating temperatures**

Metal components with different wear thicknesses ranging from 2 mm to 5 mm were heated to temperatures of 20 °C, 40 °C, 60 °C, 80 °C, 100 °C, 120 °C, 140 °C, and 160 °C, respectively. Temperature calculation formulas for metal components with varying wear thicknesses at different heating temperatures were established, as shown in Fig. 6. This laid the foundation for training and predicting simulation data using BP neural networks.

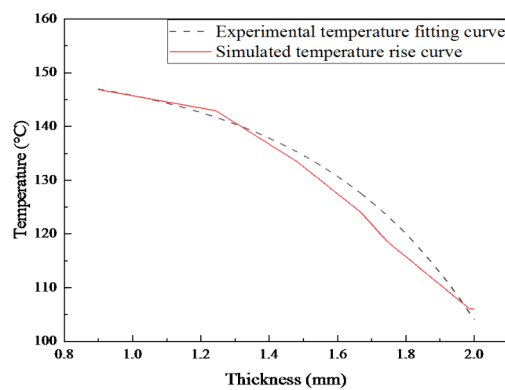
As can be seen from Fig. 6, as the heating temperature continues to increase, the slope of the fitted temperature curve for the worn and unworn areas of the metal component gradually steepens, and the temperature difference between them also gradually widens.

**Training of BP neural network model and wear prediction  
Neural network structure for damage prediction of metal components**

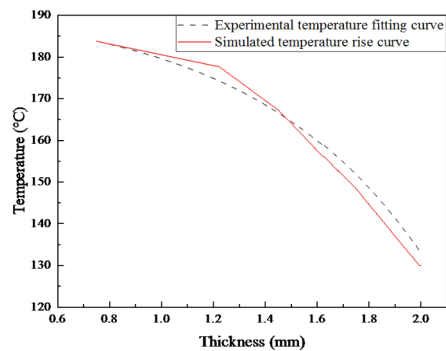
A neural network is an abstract mathematical model that connects multiple neurons in a certain topological structure. It possesses a high degree of nonlinear mapping capability, robust parallel computing power, and



(a)



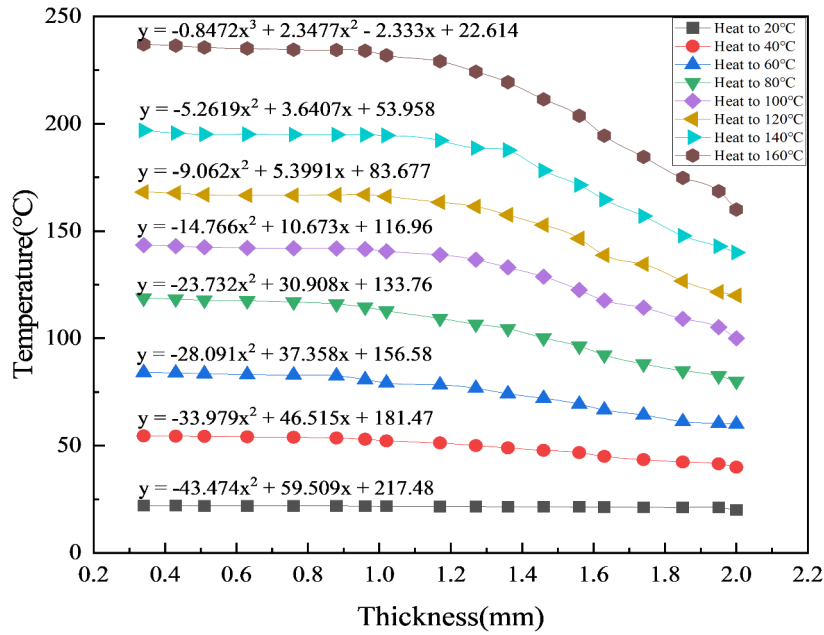
(b)



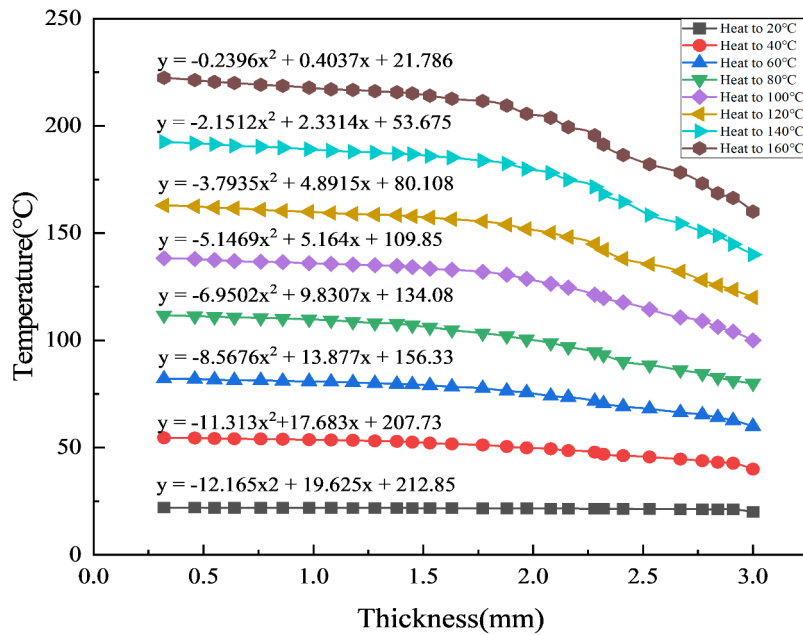
(c)

**Fig. 5.** Simulation and fitting of temperature rise curves for 2 mm miter wear plates under different heating temperatures. (a) Heating to 80 degrees Celsius simulated and Fitting experimental temperature rise curves. (b) Heating to 106 degrees Celsius simulated and experimental temperature rise curves. (c) Heating to 130 degrees Celsius simulated and Fitting experimental temperature rise curves.

adaptive learning ability. The neural network trains itself using input samples and target output samples. After each training session, the output value is compared with the target sample. If the output does not meet the specified error accuracy, this information is fed back to each neural layer. Based on the selected algorithm, each neural layer will adjust its weights and thresholds to enable the network to establish the specified nonlinear



(a)

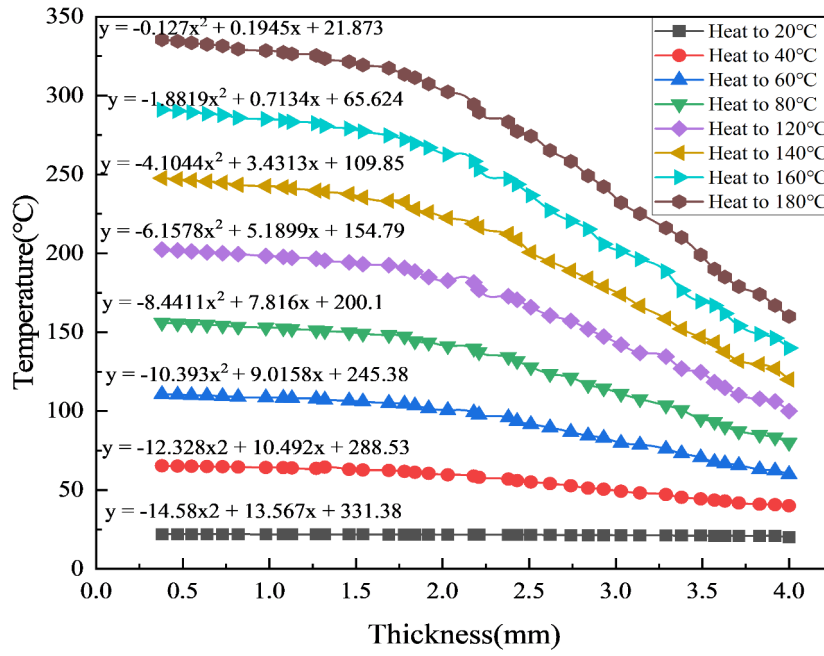


(b)

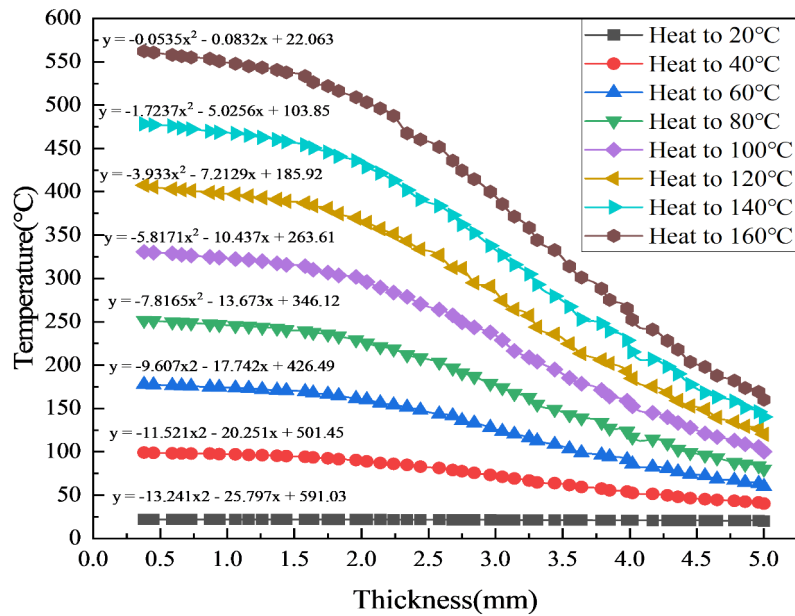
**Fig. 6.** Temperature of metal components corresponding to different wear thicknesses under different heating temperatures. (a) 2 mm miter wear metal members at different heating temperatures. (b) 3 mm miter wear metal members at different heating temperatures. (c) 4 mm miter wear metal members at different heating temperatures. (d) 5 mm miter wear metal members at different heating temperatures.

mapping relationship between input and output. A well-trained BP neural network possesses generalization capability, capable of providing appropriate outputs for inputs not included in the sample set.

The design of this model employs a BP neural network with 2 input layers, 10 hidden layers, and 1 output layer, as illustrated in Fig. 7.



(c)



(d)

Figure 6. (continued)

Among them,  $W_{ij}$  represents the connection weights between the input layer and the hidden layer, while  $V_j$  denotes the connection weights between the hidden layer and the output layer. Typically, the training data and prediction data are set in an 8:2 ratio. In this study, a two-factor process experiment was designed, and all data measured from both experiments and simulations were used for model training.

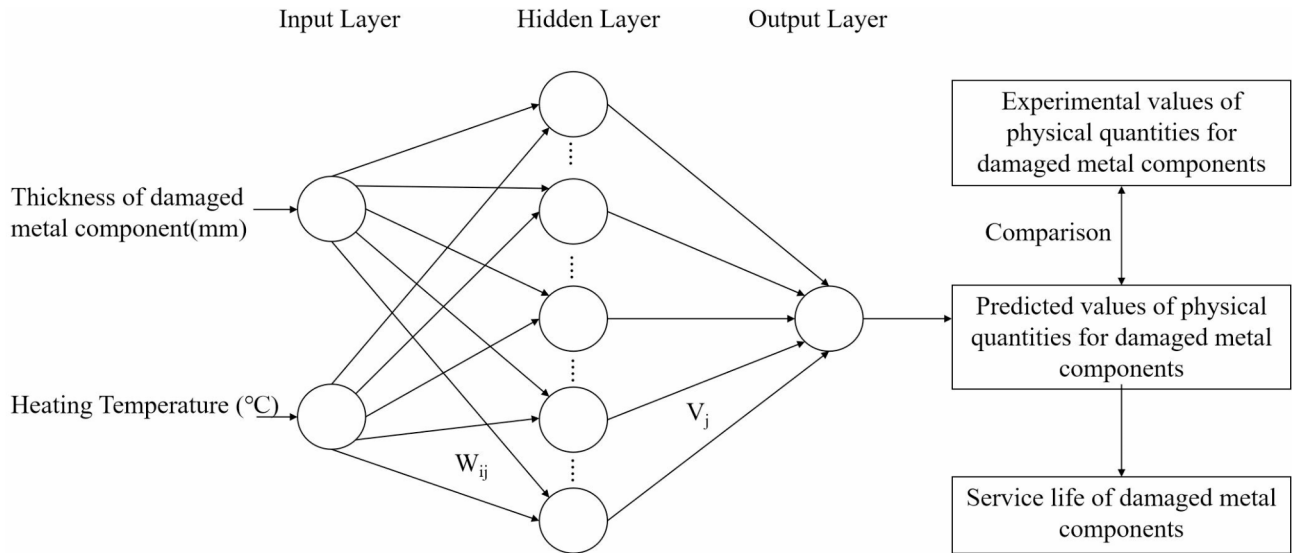


Fig. 7. Wear prediction model based on BP neural network.

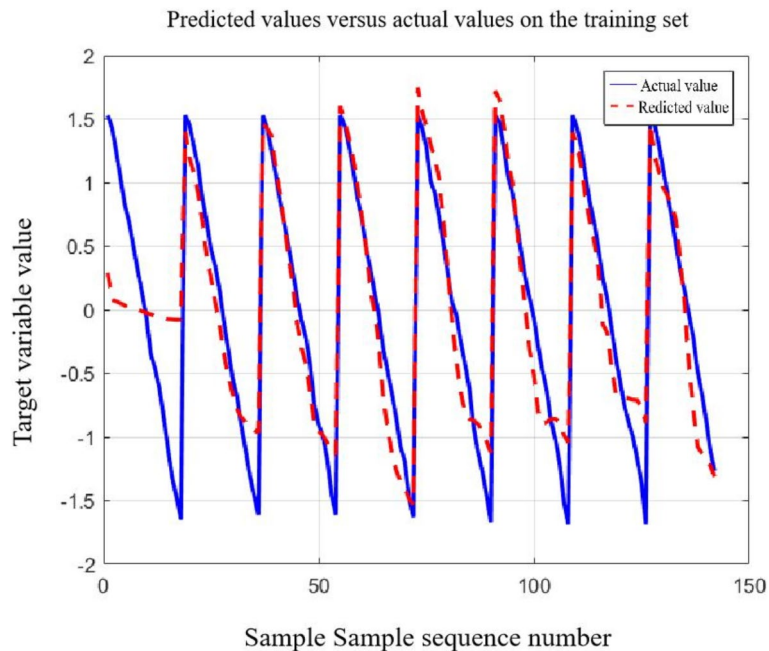


Fig. 8. Training diagram of 2 mm simulation data.

**Training and prediction of BP neural network model**

The target function values obtained through finite element simulation software are used as learning samples to train the neural network model established above. We set 80% of the data derived from the simulation software as the training set and the remaining 20% as the test set. The training parameters are configured with the number of iterations epochs set to 1000, the error threshold goal set to  $1e-6$ , and the learning rate  $lr$  set to 0.01.

The simulated data for 2 mm metal components, after 1000 iterations of training and weight adjustments, achieved a mean squared error of 0.0021344 for the network, with a coefficient of determination  $R^2$  of 0.35336. The training is now complete. The training plot for the 2 mm simulated data is shown in Fig. 8, and the prediction plot is shown in Fig. 9.

The simulated data for 3 mm metal components, after undergoing 1,500 iterations of training and weight adjustments, achieved a mean squared error of 0.0050133 for the network. The coefficient of determination  $R^2$  was 0.96115. The training was completed. The training plot for the 3 mm simulated data is shown in Fig. 10, and the prediction plot is shown in Fig. 11.

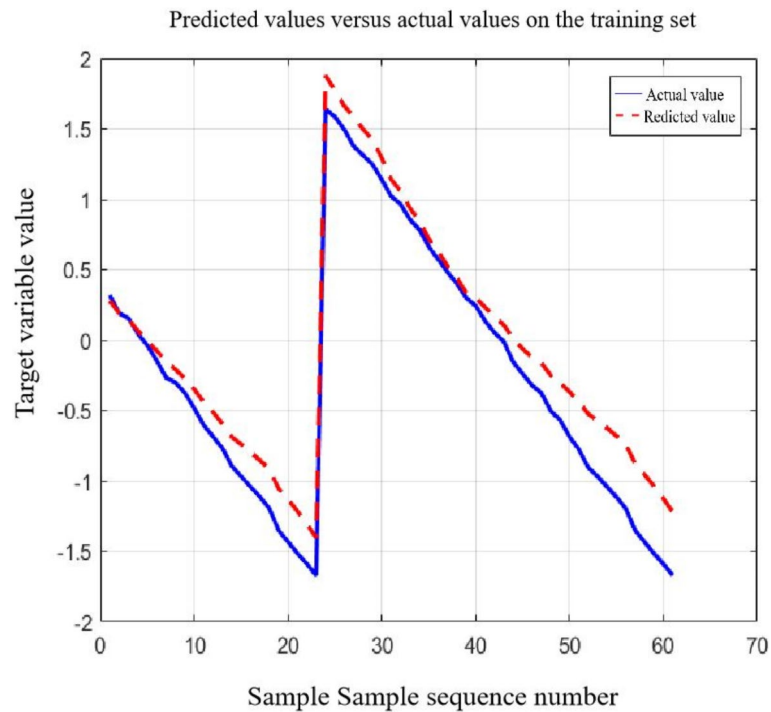


Fig. 9. Prediction of 2 mm simulated data.

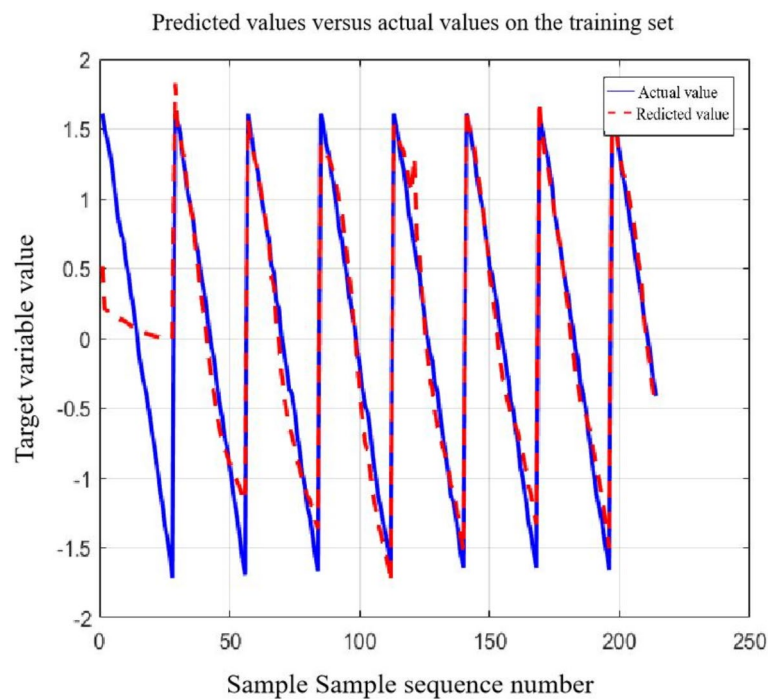


Fig. 10. Training diagram of 3 mm simulation data.

The simulated data for 4 mm metal components, after undergoing 1,300 iterations of training and subsequent weight adjustments, achieved a mean squared error of 0.0010381 for the network. The coefficient of determination  $R^2$  was 0.98324. The training was completed. The training plot for the 4 mm simulated data is shown in Fig. 12, and the prediction plot is shown in Fig. 13.

The simulated data for 5 mm metal components, after undergoing 1000 training iterations and weight adjustments, achieved a mean squared error of 0.020887 for the network. The coefficient of determination  $R^2$

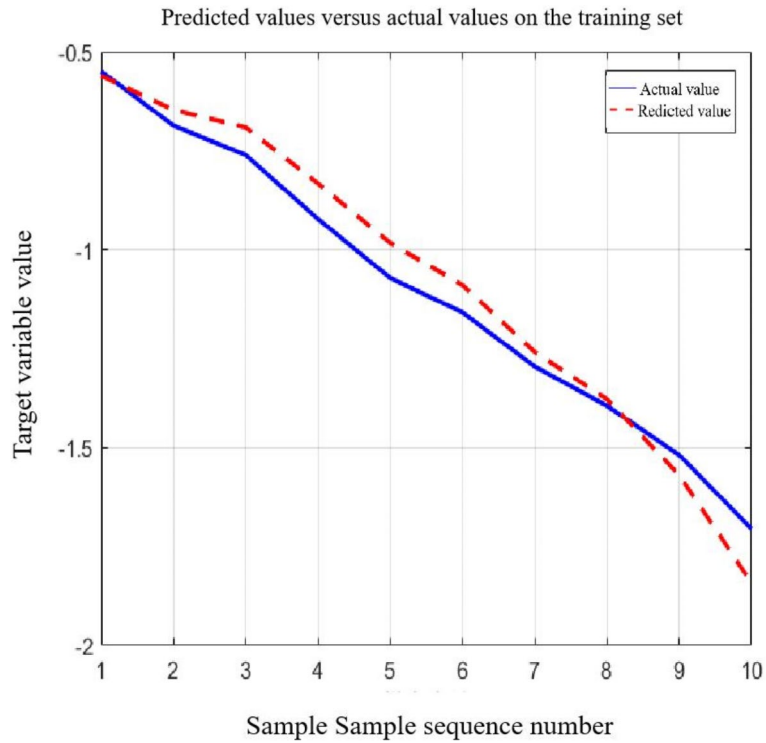


Fig. 11. Prediction of 3 mm simulated data.

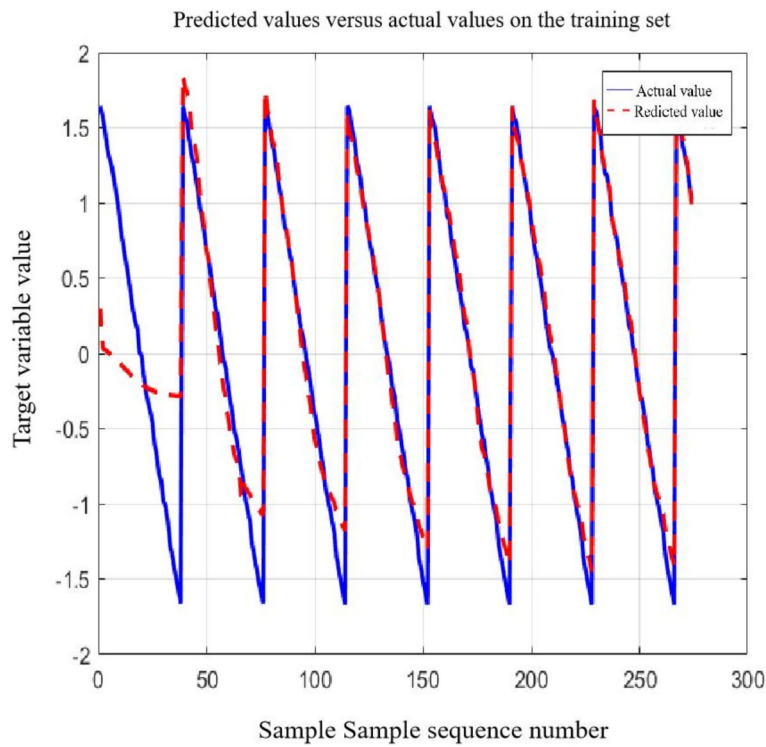


Fig. 12. Training diagram of 4 mm simulation data.

was 0.97591. The training was completed. The training plot for the 5 mm simulated data is shown in Fig. 14, and the prediction plot is shown in Fig. 15.

Under different thicknesses of metal components, the predicted values output by the neural network model exhibited a high degree of consistency with the actual values obtained through precise measurements. This

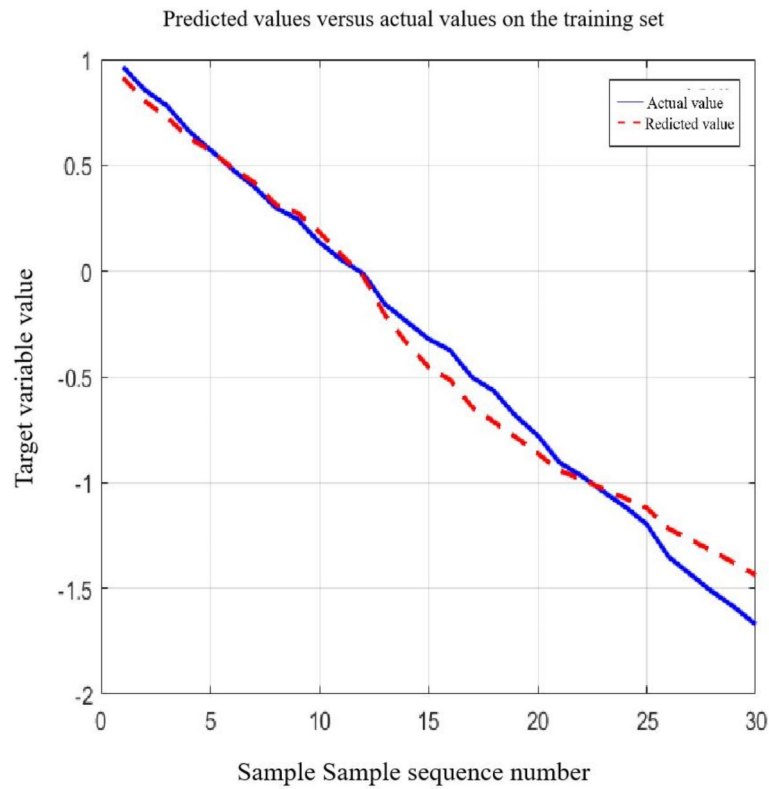


Fig. 13. Prediction of 4 mm simulated data.

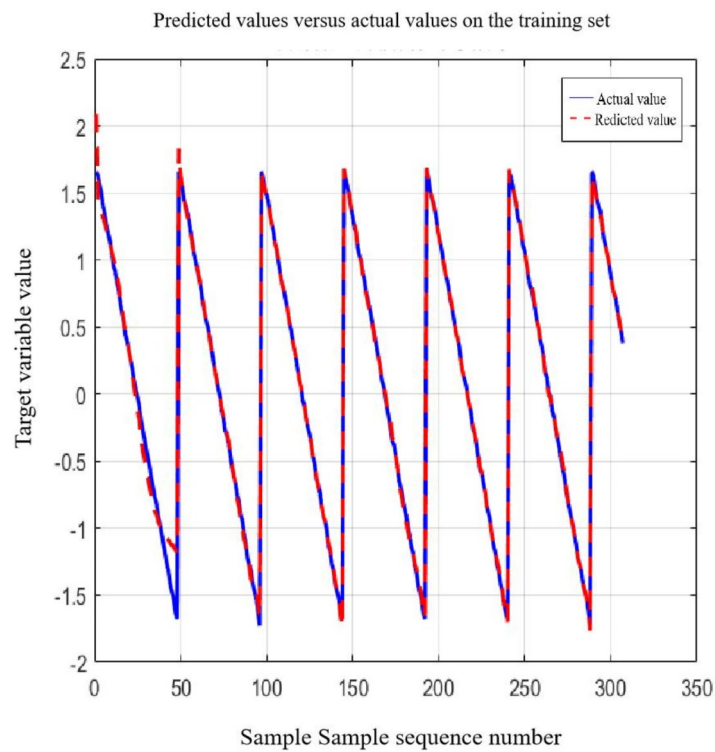
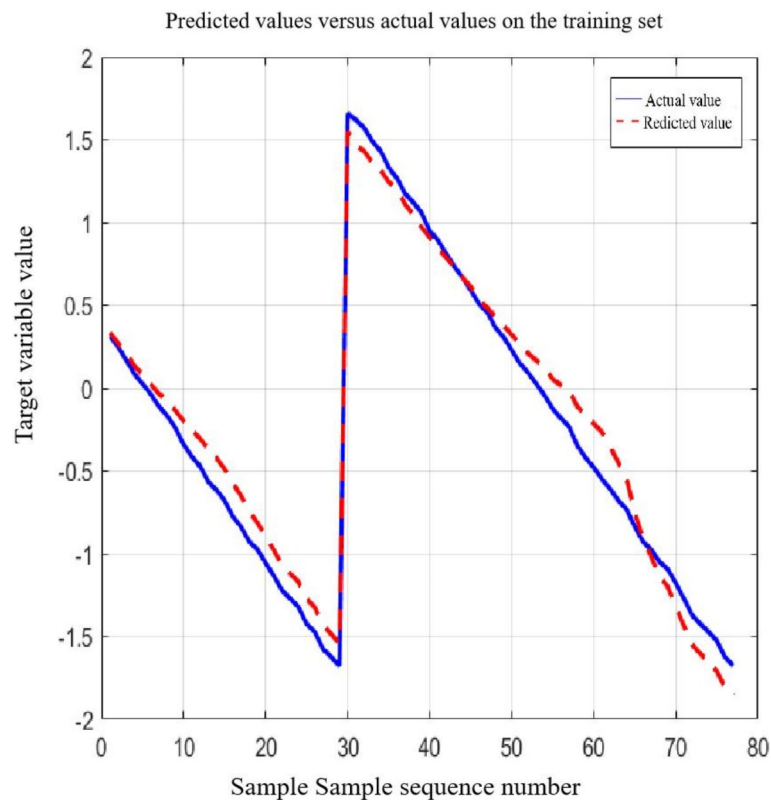


Fig. 14. Training diagram of 5 mm simulation data.



**Fig. 15.** Training diagram of 5 mm simulation data.

consistency is not only reflected in the numerical closeness but also in the alignment of trends and distribution patterns. This finding strongly validates the feasibility and potential of BP (Back Propagation) neural networks in rapidly and accurately detecting the damage thickness of metal components. Leveraging its powerful nonlinear mapping ability and self-learning capability, the BP neural network can efficiently handle complex damage detection tasks, thereby significantly improving detection efficiency while ensuring detection accuracy. The results of this study not only provide solid experimental evidence for the application of BP neural networks in the field of metal component damage detection but also open up new ideas for the widespread application of neural network technology in engineering. It serves as a reference for the application of rapid detection technology using neural networks for the thickness of damaged metal components in the engineering field.

## Conclusion

- (1) By setting the excitation temperature to 80°C, 105°C and 130°C, the temperature fitting curve equation is established, and the mathematical relationship of “excitation temperature-metal thickness” is obtained.
- (2) Under consistent conditions such as heating temperature, ambient temperature, and thermal conductivity, numerical simulations were combined with infrared thermal wave experiments. The research showed that the simulated temperature rise curve basically coincided with the experimental temperature fitting curve, indicating that numerical simulations can serve as a substitute for experiments.
- (3) Through numerical simulation of “excitation temperature-metal thickness” database in the proportion of 8:2 training and prediction, found after training prediction data and the actual data, achieved the purpose of BP neural network to rapid detection of defect metal thickness, for the subsequent optimization of neural network structure and parameters, in order to improve the model prediction accuracy and generalization ability, combined with the Internet of things technology, realize the remote monitoring and data analysis, improve the monitoring efficiency and accuracy to lay the foundation.

## Data availability

Data is provided within the manuscript or supplementary information files.

Received: 19 November 2024; Accepted: 10 February 2025

Published online: 17 February 2025

## References

1. Golański, K. M. et al. Experimental study of thermomechanical behaviour of Gum Metal during cyclic tensile loadings: the quantitative contribution of IRT and DIC. *Quant. InfraRed Thermogr. J.*, 1–18. (2023).

2. Zhang, D., Zhan, C., Chen, L., Wang, Y. & Li, G. Review of unmanned aerial vehicle infrared thermography (UAV-IRT) applications in building thermal performance: towards the thermal performance evaluation of building envelope. *Quant. InfraRed Thermogr. J.* 1–31. (2024).
3. da Rosa, S. E., Neves, E. B., Martinez, E. C. & Marson, R. A. & Machado de Ribeiro dos Reis, V. M. Association of metabolic syndrome risk factors with activation of brown adipose tissue evaluated by infrared thermography. *Quant. InfraRed Thermogr. J.* 1–17. (2023).
4. Melada, J., Arosio, P., Gargano, M. & Ludwig, N. Automatic thermograms segmentation, preliminary insight into spilling drop test. *Quant. InfraRed Thermogr. J.* 1–15. (2023).
5. de Souza, M. P. V., López, F. & Maldague, X. Corrosion under insulation mitigation by passive multivariate thermography. *Quant. InfraRed Thermogr. J.* 1–13. (2024).
6. Mishra, V., Rath, S. K. & Mohapatra, D. P. Thermograms-based detection of cancerous tumors in breasts applying texture features. *Quant. InfraRed Thermogr. J.* 1–26. (2023).
7. Felczak, M. et al. Electrothermal analysis of a TEC-less IR microbolometer detector including self-heating and thermal drift. *Quant. InfraRed Thermogr. J.* 1–25. (2023).
8. Ferrarini, G., Bison, P., Bortolin, A., Cadelano, G., Garbin, E., Natali, M., Tamburini, S. Thermography for assessing the thermal performance of innovative geopolymeric radiant panels. *Quant. InfraRed Thermogr. J.* 1–17. (2023).
9. Vinnichenko, N., Pushtae, A., Plaksina, Y. & Uvarov, A. Infrared thermography applied to the surface pressure measurements in insoluble surfactant monolayers. *Quant. InfraRed Thermogr. J.* 20 (1), 1–13 (2021).
10. Masaki, A., Nagumo, K., Oiwa, K. & Nozawa, A. Feature analysis for drowsiness detection based on facial skin temperature using variational autoencoder: a preliminary study. *Quant. InfraRed Thermogr. J.* 20 (5), 304–318 (2022).
11. Bison, P. et al. Ermanno Grinzato and the humidity assessment in porous building materials: retrospective and new achievements. *Quant. InfraRed Thermogr. J.* 1–24. (2023).
12. Yu Jian, Li, H. Technical renovation of paste fill System for the Main West Orebody at Qianbixi Copper Mine. *Min. Res. Dev.* 43 (04), 18–22. <https://doi.org/10.13827/j.cnki.kyyk.2023.04.032> (2023).
13. Longjian, B., Guochao, Y. & Tao, Y. Study on the Properties of Fluorogypsum-Modified High-Water Fly Ash Composite Filling Material. *Min. Saf. Environ. Prot.*, 47(06): 32–36. <https://doi.org/10.19835/j.issn.1008-4495.2020.06.006>. (2020).
14. Wang Xiaolin, G. et al. Wear mechanism of high-concentration filling pipelines based on Aggregate Migration [J/OL]. *Chin. J. Nonferrous Met. Res. Appl.* 1–15. (2024)..
15. Yingjie, C. et al. Wear mechanism and parameter optimization of Paste pipelines Containing Coarse aggregates. *J. Cent. South. Univ.* 55 (01), 307–316 (2024).
16. Wang Zhongchang, C. et al. Erosion wear analysis of filling slurry on reducing pipes. *J. Shandong Univ. Sci. Technol.* 41 (04), 39–46. <https://doi.org/10.16452/j.cnki.sdkjzk.2022.04.005> (2022).
17. Zhu Xin, W. et al. Simulation Study on Resistance and wear of Tailings cemented filling Slurry Transportation pipelines. *Min. Res. Dev.* 42 (03), 120–124. <https://doi.org/10.13827/j.cnki.kyyk.2022.03.011> (2022).
18. Guo Mochuan, T. et al. Analysis of gravity Pipeline Transportation and Pipeline wear in an Iron Ore Mine. *Min. Metall. Eng.* 42 (05), 39–43 (2022).
19. Moreira, N. M., Carrasquila, A. A., Figueiredo, A. & Fonseca CE. *Worn Pipes Collapse Strength* Experimental and numerical study. *J. Pet. Sci. Eng.* 133328–334. (2015).
20. Hu, R., Zhang, Y. & Wang, L. Research on evaluation of university emergency management ability based on BP neural network. *Int. J. Environ. Res. Public Health.* 20 (5), 3970 (2023).
21. Gu Fanji. Computational Neuroscience Research on Grid cells. *Sci. China.* 67 (03), 17–21 (2015).
22. Dang Weiben, W. & Wang, Y. Yan, et al. Optimization of Reduction Roasting-Magnetic Separation Process Conditions for Lateritic Nickel Ore Based on BP Neural Network Technology. *Conserv. Utilization Mineral. Resour.*, 40(05): 128–133. DOI: <https://doi.org/10.13779/j.cnki.issn1001-0076.2020.05.017>. (2020).
23. Alnaggar, M. Bhanot N. Engineering Fracture Mechanics. 197, 160. (2018).
24. Song Ming, L. et al. *Chin. J. Theor. Appl. Mech.*, 52(1), 82. (2020).
25. Zhang Lingyun, S. et al. Prediction of Springback in Aircraft Rib Rubber bladder forming based on RBF neural network. *J. Plast. Eng.* 28 (05), 218–225 (2021).
26. Xie Peng, L. et al. *Inspection Integr.*, 40(6), 651. (2021).
27. Chu Linhua, Z. et al. Rolling damage prediction of Zirconium Alloy tubes for Nuclear Use based on improved BP Network with Finite element and fireworks Algorithm. *Mater. Rev.* 37 (S1), 449–455 (2023).
28. Guo, H. et al. Tool wear Prediction Combining Feature Fusion and BP neural network [J/OL]. *Mach. Des. Manuf.* 1–5. (2024).
29. Zhang Yue, Z. et al. A tire wear detection Algorithm based on BP neural network. *Electr. Autom.* 45 (01), 109–112 (2023).
30. Huang Yao, S. & Xianping, W. Leigang, et al. Wear prediction of Extrusion dies based on BP neural network. *J. Plast. Eng.* (02): 64–66. (2006).
31. Zhang, W. Li Kangning, Wang Weiran, et al. Analysis of high-speed milling surface topography and prediction of wear resistance. *Materials.* 15(5), 1707. (2022).
32. Cao, Y. Zhao Ji, Qu Xingtian, et al. Prediction of abrasive belt wear based on BP neural network. *Machines* 9(12), 314. (2021).
33. Hua, A. & Guofeng, W. Tool Condition monitoring and remaining useful life prediction Method based on deep learning theory. *J. Electron. Meas. Instrum.* 33 (09), 64–70. <https://doi.org/10.13382/j.jemi.B1902208> (2019).
34. Zhao, B., Li, S., Gao, D., Xu, L. & Zhang, Y. Research on intelligent prediction of hydrogen pipeline leakage fire based on Finite Ridgelet neural network. *Int. J. Hydrog. Energy* 47 (55), 23316–23323. <https://doi.org/10.1016/j.ijhydene.2022.05.124> (2022).
35. Zhao, B., Chen, H., Gao, D. & Xu, L. Risk assessment of refinery unit maintenance based on fuzzy second generation curvelet neural network. *Alex. Eng. J.* 59 (3), 1823–1831. <https://doi.org/10.1016/j.aej.2020.04.052> (2020).
36. Zhao, B. & Song, H. Fuzzy Shannon wavelet finite element methodology of coupled heat transfer analysis for clearance leakage flow of single screw compressor. *Eng. Comput.* 37 (3), 2493–2503. <https://doi.org/10.1007/s00366-020-01259-6> (2021).
37. Zhao, B., Ren, Y., Gao, D., Xu, L. & Zhang, Y. Energy utilization efficiency evaluation model of refining unit Based on Contourlet neural network optimized by improved grey optimization algorithm. *Energy* 185, 1032–1044. <https://doi.org/10.1016/j.energy.2019.07.111> (2019).
38. Zhao, B., Ren, Y., Gao, D. & Xu, L. Performance ratio prediction of photovoltaic pumping system based on grey clustering and second curvelet neural network, *Energy* 171, 360–371. <https://doi.org/10.1016/j.energy.2019.01.028> (2019).
39. Huo, Y. Zhang Cunlin. Quantitative infrared detection of Internal defects in Carbon Fiber Reinforced Polymer composites. *Acta Phys. Sin.* 61 (14), 199–205 (2012).
40. Wang Qiang, H. et al. Differential Laser Infrared Thermography for Internal Defect Detection in Aerospace Composite materials. *Infrared Laser Eng.* 48 (05), 127–133 (2019).

## Author contributions

Chunming Ai: Conceptualization, Methodology, Project administration, Resources, Writing- review & editing. Haichuan Lin: Data curation, Supervision, Writing- original draft, Writing- review & editing. Pingping Sun: Supervision.

## Funding

This work was supported by the Natural Science Foundation Program of Liaoning Province (No. 2022-MS-395) and National Natural Science Foundation of China (51604138).

## Declarations

## Competing interests

The authors declare no competing interests.

## Additional information

**Correspondence** and requests for materials should be addressed to H.L.

**Reprints and permissions information** is available at [www.nature.com/reprints](http://www.nature.com/reprints).

**Publisher's note** Springer Nature remains neutral with regard to jurisdictional claims in published maps and institutional affiliations.

**Open Access** This article is licensed under a Creative Commons Attribution-NonCommercial-NoDerivatives 4.0 International License, which permits any non-commercial use, sharing, distribution and reproduction in any medium or format, as long as you give appropriate credit to the original author(s) and the source, provide a link to the Creative Commons licence, and indicate if you modified the licensed material. You do not have permission under this licence to share adapted material derived from this article or parts of it. The images or other third party material in this article are included in the article's Creative Commons licence, unless indicated otherwise in a credit line to the material. If material is not included in the article's Creative Commons licence and your intended use is not permitted by statutory regulation or exceeds the permitted use, you will need to obtain permission directly from the copyright holder. To view a copy of this licence, visit <http://creativecommons.org/licenses/by-nc-nd/4.0/>.

© The Author(s) 2025